PHYSICAL REVIEW D

PARTICLES AND FIELDS

THIRD SERIES, VOLUME 25, NUMBER 5 1 MARCH 1982

Study of single-pion production by weak charged currents in low-energy νd interactions

G. M. Radecky,* V. E. Barnes, D. D. Carmony, and A. F. Garfinkel
Purdue University, West Lafayette, Indiana 47907

M. Derrick, E. Fernandez, L. Hyman, G. Levman,† D. Koetke,‡
B. Musgrave, P. Schreiner,§ R. Singer,§ A. Snyder,|| and S. Toaff¶
Argonne National Laboratory, Argonne, Illinois 60439

S. J. Barish,** A. Engler, R. W. Kraemer,
K. Miller,†† and B. J. Stacey‡‡
Carnegie-Mellon University, Pittsburgh, Pennsylvania 15213

R. Ammar, D. Coppage, D. Day, R. Davis, N. Kwak, and R. Stump
Carnegie-Mellon University, Pittsburgh, Pennsylvania 15213
(Received 14 September 1981)

This paper gives the results of a study of single-pion production by the weak charged current utilizing the wide-band muon-type-neutrino beam at the Argonne Zero Gradient Synchrotron. The data were obtained from hydrogen and deuterium fillings of the 12-ft bubble chamber. The methods of event selection and separation from background are given as are the details of the corrections and systematic effects in the data sample. The energy-dependent cross sections and differential distributions are presented for the three single-pion production reactions $\nu p \to \mu^- p \pi^+$, $\nu n \to \mu^- p \pi^0$, and $\nu n \to \mu^- n \pi^+$. An isospin decomposition shows that the ratio of $I=\frac{1}{2}$ to $I=\frac{3}{2}$ amplitudes is 0.68 ± 0.04 with a relative phase of $(90.7 \pm 4.6)^\circ$ for $M(N\pi) < 1.4$ GeV. This agrees with theoretical models, particularly the detailed calculation of Adler. Using the data of the reaction $\nu p \to \mu^- p \pi^+$, the characteristic mass of the nucleon axial-vector elastic form factor is measured to be $0.98^{+0.06}_{-0.03}$ GeV when analyzed within the context of the Adler model. The data are also compared to other parametrizations of the nucleon axial-vector form factor.

I. INTRODUCTION

In this paper we present our final results on single-pion production in charged-current (CC) neutrino reactions from two experiments using the Argonne National Laboratory 12-ft bubble chamber. Some results from the first experiment have been published.[1] This paper reports results from a data sample more than three times as large. The experimental setup has already been described.[2] The conditions of the second experiment differ from those of the first experiment in two respects: (a) the use of higher proton intensities and (b) the addition of γ-converting plates in the downstream end of the bubble chamber for part of the exposure. The plates reduced the fiducial volume from 11.1 m^3 to 8.64 m^3. We have combined the data samples from the first and second experiments and present here our final results on single-pion production.[3]

For neutrino energies below 6 GeV, where our data are concentrated, it is currently accepted that the weak hadronic CC contains only vector and axial-vector components. The hypothesis of the isotriplet vector current directly relates the weak hadronic current to the isovector electromagnetic current. That current has been well studied in electroproduction reactions. Our experiment provides a detailed study of the weak hadronic axial-vector current.

II. EVENT SELECTION AND CORRECTIONS TO THE SINGLE-PION DATA SAMPLE

There are three neutrino interactions on deuterium which lead to single-pion production:

$$\nu d \rightarrow \mu^- p \pi^+ n_s \ , \tag{1}$$

$$\nu d \rightarrow \mu^- p \pi^0 p_s \ , \tag{2}$$

$$\nu d \rightarrow \mu^- n \pi^+ p_s \ , \tag{3}$$

where n_s and p_s are spectator nucleons. Topologically, reaction (1) is a three-prong event. In this chamber, one observed protons with momenta greater than approximately 100 MeV/c; therefore, examples of reactions (2) and (3) are found in both the two- and three-prong topologies.

All two- and three-prong events recorded in the scan were processed through the programs TVGP and SQUAW which performed the geometrical reconstruction and kinematic fitting, respectively. The events were measured several times where necessary, with a resulting reconstruction efficiency of about 92%. In the events where the spectator is unseen, momentum components p_x, p_y, and p_z were given starting values of 0 ± 50 MeV/c in the fit. Since the angles which specify the neutrino beam direction are known to an accuracy of 1°, three-constraint (3C) fits were performed to select events of reaction (1). A zero-constraint (0C) calculation was performed to select events of reactions (2) and (3).

Any two- or three-prong event that satisfied the above kinematics was reviewed by a physicist. Each event was visually checked and information such as track shape, ionization density, particle decays, and secondary interactions was used to help resolve ambiguities and to further classify the candidate events.

In addition to our requirement that the selected event assignment be consistent with the visual information, additional kinematic selection criteria were necessary to obtain a relatively background-free sample of events. These selections are as follows.

(1) The χ^2 fit probability must be $\geq 1\%$ for the $\mu^- p \pi^+ n_s$ final state.

(2) Whenever an event had a constrained fit to the reactions $\nu d \rightarrow \mu^- p \pi^+ n_s$ and/or $\nu d \rightarrow \mu^- p p_s$ with χ^2 probability $\geq 1\%$, unless the visual information was incompatible, such fits were accepted in preference to 0C solutions.

(3) For the 0C final states $\mu^- p \pi^0 p_s$ and $\mu^- n \pi^+ p_s$ the neutrino energy E_ν must be < 1.5 GeV and the spectator momentum p_s must be < 0.35 GeV/c. The neutrino-energy cut was necessary to reduce contamination from double-pion production.

(4) Additionally, for the $\mu^- n \pi^+ p_s$ final state we required that the angle between the incident neutrino and the outgoing neutron, $\theta_{\nu n}$, be $> 10°$, that the neutron-to-neutrino momentum ratio, p_n/p_ν, be < 0.9, and that the angle between the μ^- and π^+ tracks, $\theta_{\mu\pi}$, be $< 150°$. These cuts substantially reduce a background from incoming charged hadrons which scatter and satisfy the kinematics of reaction (3). No discernible bias in either the Q^2 or $N\pi$ invariant mass was introduced by these cuts when their effect on reaction (1) was studied.

After the application of the above criteria and incorporation of the visual information only 2% of the $\mu^- p \pi^+ n_s$ events had a π^+/p ambiguity between the positive tracks and this was resolved by selecting the fit with the higher χ^2 probability. About 15% of the events were ambiguous between reactions (2) and (3). This ambiguity was handled by comparing the proton and pion momentum spectra of the events uniquely assigned to these reactions. We found that if both nucleon-pion invariant-mass combinations were less than (greater than) 1.4 GeV the event was assigned to the $\mu^- p \pi^0 p_s$ final state with a weight of 0.9 (0.64). For the events where one mass interpretation is below 1.4 GeV and the other mass interpretation is above 1.4 GeV, the assigned weight was one half of the sum of the weights determined above. The neutrino-energy cut of 1.5 GeV was applied after the ambiguity resolution.

In addition to the cuts already discussed above, there are several backgrounds and also losses for reactions (1)—(3) which are listed below:

(1) The contamination in channels (1)—(3) from multipion production processes involving one or more neutral secondaries.

(2) The contamination in channels (1)—(3) from neutron interactions in the liquid and from neutrino-induced neutral-current interactions.

(3) The contamination due to photon-induced backgrounds for reactions (1)—(3).

(4) The background from unrecognized incoming charged tracks which scatter in the liquid; this occurs in all three reactions.

(5) The loss of events in reaction (2) and (3) where one or more charged particles scatter so as to make the track unmeasurable.

(6) The loss of reaction (1) due to events with high-momentum neutron spectators which fail to give a kinematical fit.

(7) The correction for nuclear rescattering effects in reactions (1)—(3) which increases the frequency of high-momentum spectators at the expense of the slower ones.

(8) The loss from $\mu^- p\pi^0 p_s$ to the final state $\mu^- pp_s$ due to overlap of the kinematics for both reactions.

The method of making these corrections which are tabulated in Table I is discussed in Ref. 1. Here, for the most part,[3] we adopt the same procedure although the corrections are more precise because of the increased population of the various channels utilized and also because improvements made to the shielding substantially reduced the neutron and charged hadron backgrounds.

The neutron background for the present experiment has been discussed elsewhere.[4] The cross sections used to correct for one-pion production by the neutral currents have been published.[4,5] Finally, double-pion production by the charged current is discussed in Ref. 6.

Most of the film was double scanned. Because the film quality deteriorated near the end of the experiment, about 10% of the film was triple scanned and the visibility approach of Derenzo and Hildebrand[7] was used to monitor the quality of the scans. We found it necessary to discard the final portion of the film. In the remainder of the film the third scan validated the conventionally calculated double-scan efficiency for the events of the three-prong topology. For those events of reactions (2) and (3) which are in the two-prong topology it was necessary to make a small correction ($\leq 5\%$) for events which were systematically missed in the final portion of the utilized film.

We have estimated the resolution in the kinematical quantities for the 0C reactions (2) and (3) using the events of reaction (1) with the appropriate track removed. We find that the resulting uncertainties in E_ν, Q^2, and $M(N\pi)$ are best described

TABLE I. Summary of rate corrections.

Reason for correction		Correction factor
	(a) $\nu d \to \mu^- p\pi^+ n_s$	
Measuring and reconstruction		1.088±0.019
Scanning efficiency		1.003±0.003
Background		0.981±0.012
Loss of fast-neutron spectators		1.220±0.045
	(b) $\nu d \to \mu^- p\pi^0 p_s$	
Measuring and reconstruction		1.078±0.013
Scanning efficiency		1.055±0.017
Neutrino-multipion background	(5.7±1.9)%	
Neutron-induced background	(2.7±0.9)%	
Neutral-current background	(4.4±3.4)%	0.860±0.042
Photon-induced background Incident scatters	(1.2±1.2)%	
Loss of underconstrainted events		1.046±0.010
Events assigned to $\mu^- pp_s$		1.266±0.048
Spectator cut		1.106±0.036
	(c) $\nu d \to \mu^- n\pi^+ p_s$	
Measuring and reconstruction		1.078±0.013
Scanning efficiency		1.075±0.024
Neutrino-multipion background	(5.2±2.1)%	
Neutron-induced background Neutral-current background	(1.3±0.5)%	0.910±0.026
Photon-induced background Incident scatters	(2.6±1.5)%	
Loss of underconstrained events		1.050±0.010
Correction for $p_n/p_\nu > 0.9$ and $\theta_{\nu n} < 10°$		1.030±0.007
Correction for $\theta_{\mu\pi} > 150°$		1.059±0.011
Spectator cut		1.106±0.036

TABLE II. Resolutions for the 0C single-pion reactions.

Quantity	$\nu d \to \mu^- p \pi^0 p_s$	$\nu d \to \mu^- n \pi^+ p_s$
E_ν (GeV)	0.050	0.030
Q^2 [(GeV/c)^2]	0.020	0.015
$M(N\pi)$ (GeV)	0.030	0.010

by Breit-Wigner line shapes whose characteristic widths are tabulated in Table II. They range from 10 to 50 MeV.

The complete data sample with the above discussed selections and corrections consists of 1115.0 (871) $\mu^- p \pi^+$, 272.8 (202.2) $\mu^- p \pi^0$, and 255.8 (206.2) $\mu^- n \pi^+$ corrected (raw) events.

III. PHYSICS OF SINGLE-PION PRODUCTION

A. General properties of the $\mu^- p \pi^+$, $\mu^- p \pi^+$, and $\mu^- n \pi^+$ final states

We now present the data for the three single-pion production reactions. Figures 1—3 display the nucleon-pion, nucleon-muon, and muon-pion invariant-mass combinations, respectively. It is apparent that the $\mu^- p \pi^+$ final state is dominated by $\Delta^{++}(1232)$ production with few events at high mass. That high-mass final states are kinematically allowed can be seen in the nucleon-muon distributions of Fig. 2. In contrast to the situation for the $\mu^- p \pi^+$ final state, it is not obvious that Δ pro-

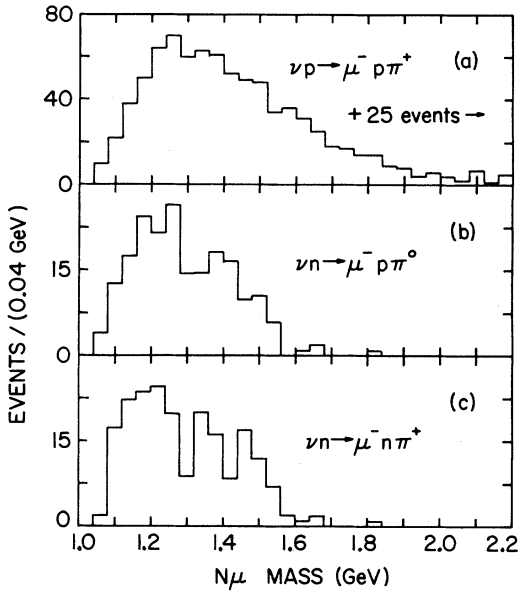

FIG. 2. The nucleon-muon ($N\mu$) invariant-mass distributions for the final states (a) $\mu^- p \pi^+$, (b) $\mu^- p \pi^0$, and (c) $\mu^- n \pi^+$.

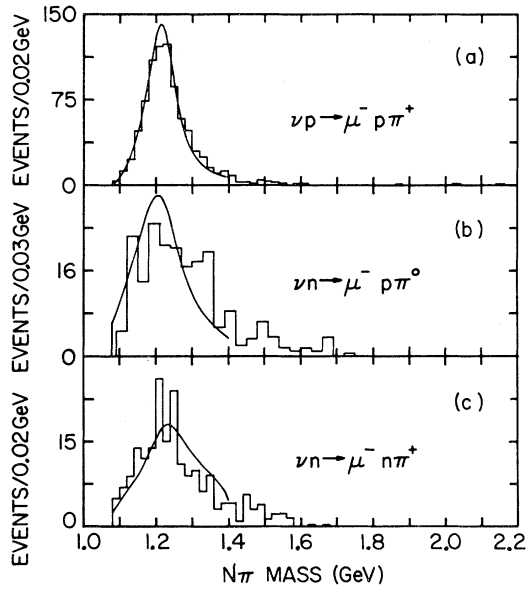

FIG. 1. The nucleon-pion ($N\pi$) invariant-mass distributions for the final states (a) $\mu^- p \pi^+$, (b) $\mu^- p \pi^0$, and (c) $\mu^- n \pi^+$. The curves are the area-normalized predictions of the Adler model folded with the experimental resolution function.

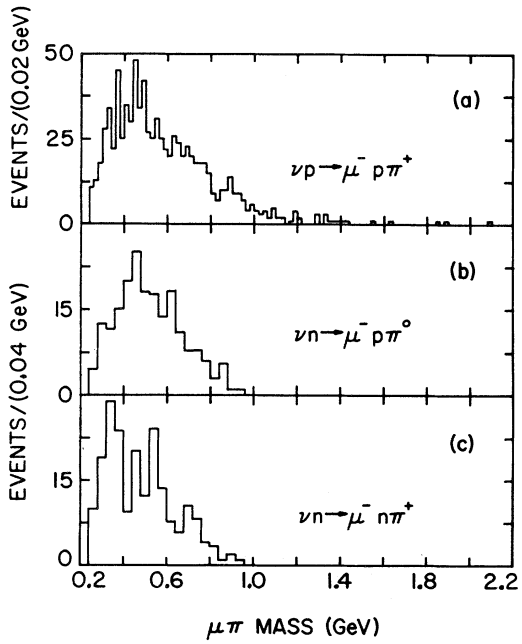

FIG. 3. The muon-pion ($\mu\pi$) invariant-mass distributions for the final states (a) $\mu^- p \pi^+$, (b) $\mu^- p \pi^0$, and (c) $\mu^- n \pi^+$.

duction dominates the $\mu^- p\pi^0$ and $\mu^- n\pi^+$ final states. In particular, there is more evidence for high-mass nucleon-pion final states than is seen for reaction (1) even though these data are limited to $E_\nu < 1.5$ GeV. Our study of the reaction $\bar{\nu}p \rightarrow \mu^+ p\pi^-$ with high-energy antineutrinos showed that the final state was dominated by the production of $I = \frac{1}{2}$ nucleon isobars.[8]

Figure 4 displays the distribution in the cosine of the neutrino-muon scattering angle θ^*, as measured in the neutrino-nucleon rest frame. The corresponding four-momentum transfer squared Q^2 distribution is shown in Fig. 5. The events satisfying the selection $M(N\pi) < 1.4$ GeV are shown cross-hatched. The forward peaking of the μ^- comes entirely from the events above 1 GeV neutrino energy. This effect is clearly exhibited in Fig. 6, which is a scatter plot of $\cos\theta^*$ versus the neutrino energy for the final state $\mu^- p\pi^+$. It is clear that near threshold, the production angular distribution of the hadronic system is nearly isotropic.

The beam energy distributions of the events shown in Fig. 7 peaks near 0.9 GeV. The corresponding cross sections are displayed in Fig. 8 and listed in Table III. The cross-section errors contain both an overall normalization uncertainty

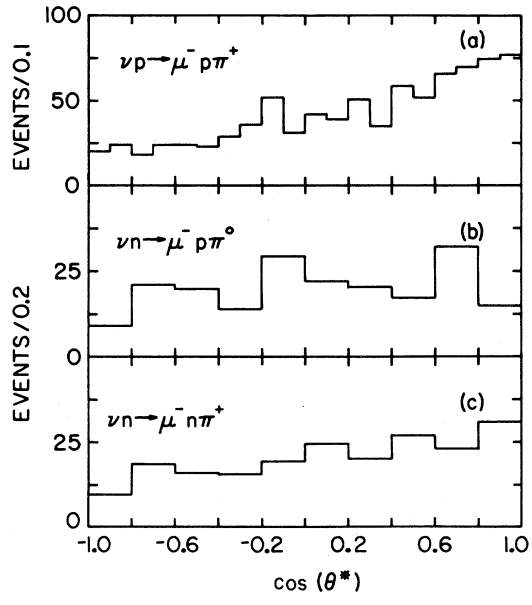

FIG. 4. The neutrino-muon scattering-angle $\cos\theta^*$ distributions as measured in the neutrino-nucleon rest frame for the final states (a) $\mu^- p\pi^+$, (b) $\mu^- p\pi^0$, and (c) $\mu^- n\pi^+$.

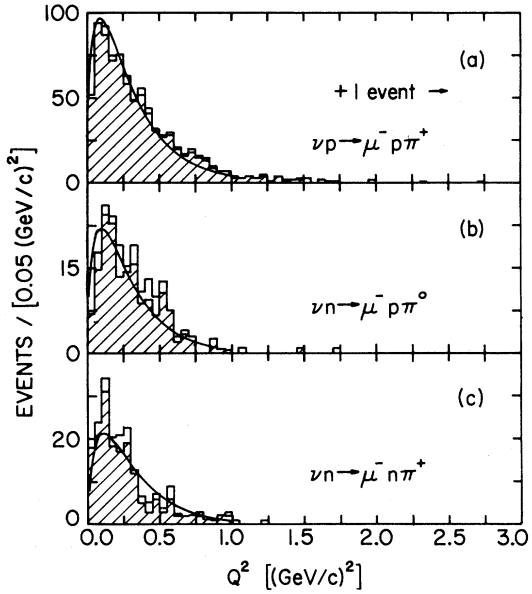

FIG. 5. The distribution in four-momentum transfer squared for the final states (a) $\mu^- p\pi^+$, (b) $\mu^- p\pi^0$, and (c) $\mu^- n\pi^+$. The cross-hatched events are those which result from the selection $M(N\pi) < 1.4$ GeV. The curves are the predictions of the Adler model area-normalized to the cross-hatched events.

of $\pm 15\%$ in the energy range $0.5-1.5$ GeV and $\pm 25\%$ elsewhere, and a point-to-point relative error in the flux shape of $\pm 5\%$. The flux was calculated from the measured pion production cross sections.[9]

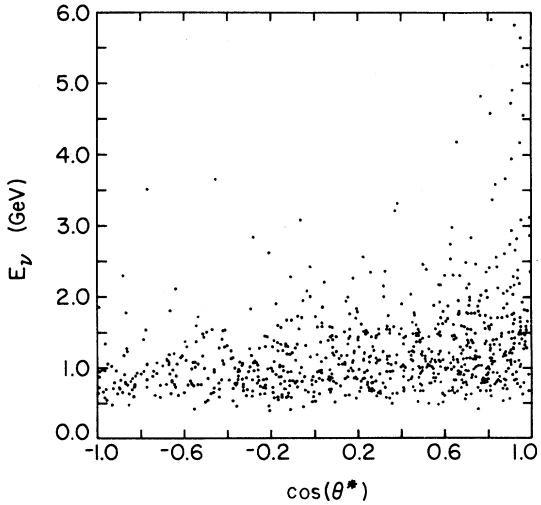

FIG. 6. Scatter plot of $\cos\theta^*$ vs E_ν for events of the $\mu^- p\pi^+$ final state.

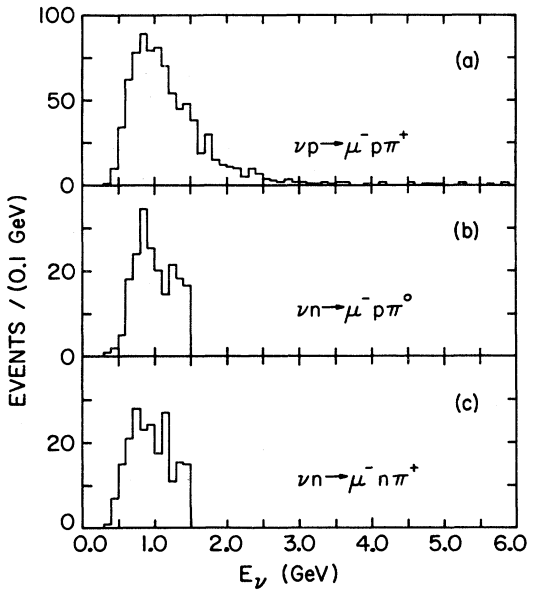

FIG. 7. The distribution of events in neutrino energy E_ν for the final states (a) $\mu^- p\pi^+$, (b) $\mu^- p\pi^0$, and (c) $\mu^- n\pi^+$. For the latter two reactions, the data are cut off at $E_\nu = 1.5$ GeV.

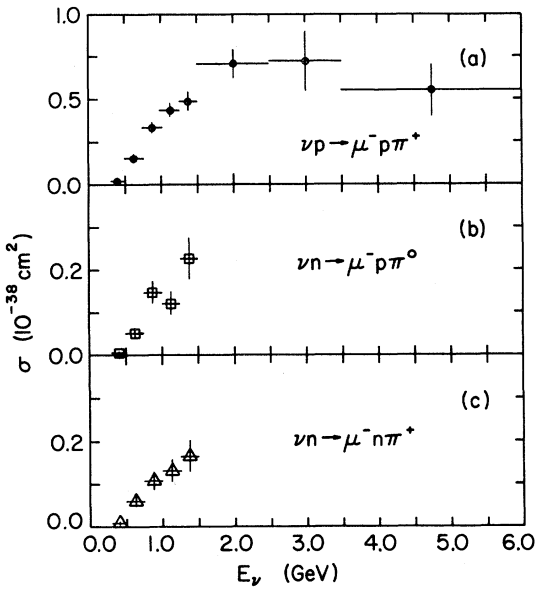

FIG. 8. The excitation functions without mass cut for the final states (a) $\mu^- p\pi^+$, (b) $\mu^- p\pi^0$, and (c) $\mu^- n\pi^+$.

TABLE III. Energy dependence of the single-pion cross sections (in units of 10^{-38} cm^2).

E_ν (GeV)	No mass cut	$M_{N\pi} < 1.4$ GeV	$M_{N\pi} < 1.6$ GeV
	(a) $\sigma(\nu p \to \mu^- p\pi^+)$		
0.3 −0.5	0.019±0.006	0.019±0.006	0.019±0.006
0.5 −0.75	0.155±0.017	0.155±0.017	0.155±0.017
0.75−1.00	0.335±0.030	0.332±0.030	0.335±0.030
1.00−1.25	0.435±0.042	0.427±0.041	0.435±0.042
1.25−1.50	0.488±0.055	0.455±0.053	0.438±0.055
1.50−2.50	0.707±0.087	0.614±0.078	0.683±0.085
2.50−3.50	0.722±0.174	0.650±0.164	0.722±0.174
3.50−6.00	0.552±0.150	0.368±0.121	0.515±0.145
	(b) $\sigma(\nu n \to \mu^- p\pi^0)$		
0.3 −0.5	0.006±0.004	0.006±0.004	0.006±0.004
0.5 −0.75	0.052±0.012	0.052±0.012	0.052±0.012
0.75−1.00	0.147±0.025	0.143±0.025	0.147±0.025
1.00−1.25	0.121±0.027	0.097±0.023	0.118±0.026
1.25−1.50	0.227±0.048	0.130±0.034	0.190±0.043
	(c) $\sigma(\nu n \to \mu^- n\pi^+)$		
0.3 −0.5	0.009±0.005	0.009±0.005	0.009±0.005
0.5 −0.75	0.061±0.012	0.061±0.012	0.061±0.012
0.75−1.00	0.109±0.020	0.105±0.019	0.109±0.020
1.00−1.25	0.132±0.026	0.098±0.021	0.132±0.026
1.25−1.50	0.166±0.037	0.112±0.030	0.162±0.037

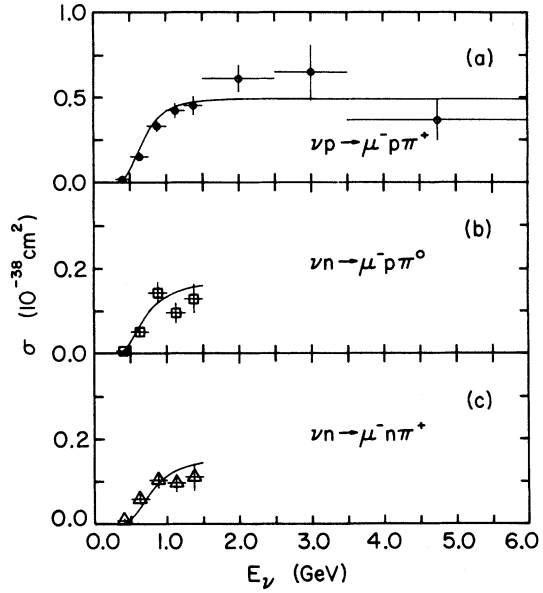

FIG. 9. The excitation functions for the final states (a) $\mu^-p\pi^+$, (b) $\mu^-p\pi^0$, and (c) $\mu^-n\pi^+$ with the selection $M(N\pi)<1.4$ GeV. The curves are the predictions of the Adler model with $M_A=0.95$ GeV.

Figures 9 and 10 display the energy dependence of the cross section for the three single-pion reactions with the selections $M(N\pi)<1.4$ GeV and $M(N\pi)<1.6$ GeV, respectively; the data are also given in Table III. These mass selections restrict the data to regions which permit comparisons with theoretical models.

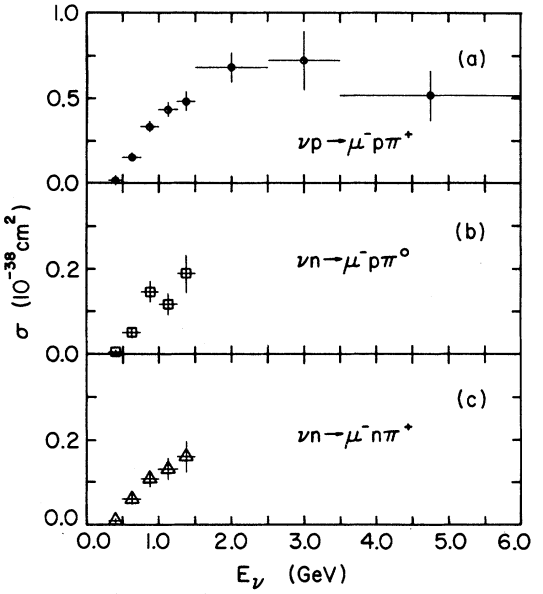

FIG. 10. The excitation functions for the final states (a) $\mu^-p\pi^+$, (b) $\mu^-p\pi^0$, and (c) $\mu^-n\pi^+$ with the selection $M(N\pi)<1.6$ GeV.

B. Determination of the axial-vector form factor from the final state $\mu^-p\pi^+$

The literature describing theoretical models of single-pion production by neutrinos is extensive.[10–13] Comparisons of experimental data with these calculations have been made over the past fifteen years.[1,14,15] The recent data give good agreement with the detailed calculations of Adler[11] and so we have chosen to compare our results with the 1975 extended Adler model. We use the extended Adler model without $O(q)$ corrections because these corrections are not well defined when the entire Δ mass region is considered. The extensions to the model made by Fogli and Nardulli[12] also agree well with the existing data.

We use our data from the final state $\mu^-p\pi^+$ with the selections $0.5\text{ GeV}<E_\nu<6.0$ GeV, $M(p\pi^+)<1.4$ GeV, to measure the characteristic mass of the axial-vector elastic form factor (M_A) using a dipole form and the Adler model. The likelihood function used is a product of a term dependent on Q^2, $W=M(N\pi)$, and the π-nucleon angular distribution; a term sensitive to the energy-dependent shape of the total cross section; and a term which depends on the energy average of the total cross section:

$$\mathscr{L}=D_1D_2D_3\ , \tag{4}$$

$$D_1=\prod_{i=1}^{N_{\text{evts}}}\frac{d^3\sigma(E_{\nu i},Q_i^2,W_i,\Omega_{\pi i},M_A)/dQ^2dW\,d\Omega_\pi}{\int\int\int d^3\sigma(E_{\nu i})}\ , \tag{5}$$

$$D_2=\prod_{j=1}^{7}\exp\{-[\sigma(j)-\sigma^R_{\text{exp}}(j)]^2/2[\Delta\sigma^R_{\text{exp}}(j)]^2\}\ , \tag{6}$$

$$D_3=\exp[-(\bar\sigma-\bar\sigma_{\text{exp}})^2/2(\Delta\bar\sigma_{\text{exp}})^2]\ . \tag{7}$$

Here $\sigma^R_{\text{exp}}(j)=\sigma_{\text{exp}}(j)(\bar\sigma/\bar\sigma_{\text{exp}})$ is the renormalized experimental cross section for bin j and $\bar\sigma$ is the flux-averaged cross section. We find

$$M_A=0.98^{+0.06}_{-0.03}\text{ GeV}$$

from the total likelihood function.

From the average-cross-section term (D_3) of the likelihood function alone we find $M_A=0.91\pm0.05$ GeV. As the Adler model was explicitly constructed for events with $Q^2<0.6$ (GeV/c)^2, we have also applied that cut to our data and find that the value

of M_A is insensitive to this cut. The value of M_A determined from the total likelihood function in this case is $M_A = 0.92^{+0.05}_{-0.06}$ GeV. Our results are in agreement with the value of $M_A = 0.95 \pm 0.09$ GeV from our direct measurement[2] using the reaction $\nu n \to \mu^- p$, as well as with the average result of 0.95 GeV obtained from other recent quasielastic scattering experiments.[16]

In the likelihood fit, we find that the broad D_1 term prefers $M_A \sim 1.25$ GeV. This behavior has also been noted by Bell *et al.*[17] In a recent paper of Sehgal[18] it was suggested that the axial-vector form factor should not be parametrized as a dipole. Following Sehgal's suggestion, we fit the axial-vector elastic form factor by the expression

$$F_A(Q^2) = (1+Q^2/m_{A_1}{}^2)^{-1} \exp\left[-\frac{1}{6}\frac{Q^2R^2}{1+Q^2/4M^2}\right]. \tag{8}$$

Using his values $m_{A_1} = \sqrt{2}m_\rho$, $R^2 = 6$ (GeV)$^{-2}$, $M = M_p$, we calculated the absolute flux-averaged predictions of the Adler model for the differential cross section $d\sigma/dQ^2$ with the selections $0.5 < E_\nu < 6.0$ GeV, $M(p\pi^+) < 1.4$ GeV. We also calculated the same quantity using the dipole form factor with the value $M_A = 0.98$ (0.95) GeV as suggested by our maximum-likelihood fit (our quasielastic result). The results are displayed in Figs. 11–13 and are tabulated in Table IV along with the model predictions and χ^2 deviation for each Q^2 bin. We also included in Table IV the measured and predicted average cross sections for all Q^2 along with its χ^2 deviation. Within our errors, both the dipole fit and the Sehgal parametrization of Eq. (8) give equally good fits.

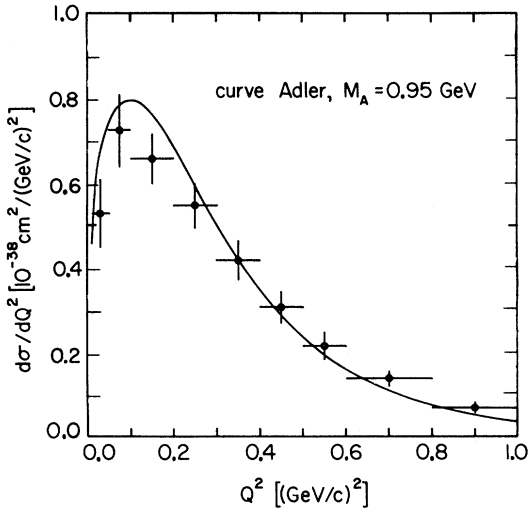

FIG. 12. Differential cross section $d\sigma/dQ^2$ evaluated with the selections $0.5 \le E_\nu < 6.0$ GeV and $M(p\pi^+) < 1.4$ GeV. The curve is the flux-averaged prediction of the Adler model with the dipole form factor and $M_A = 0.95$ GeV.

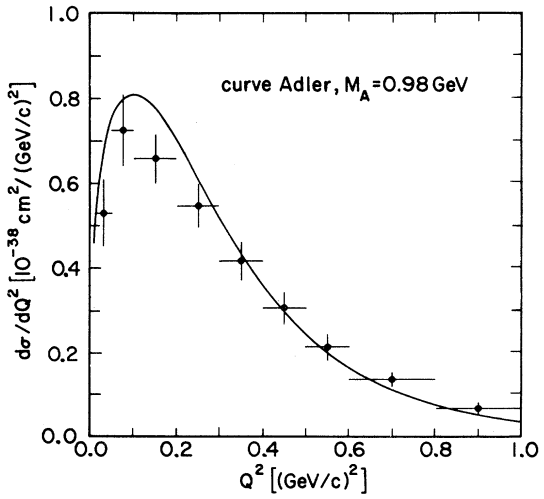

FIG. 11. Differential cross section $d\sigma/dQ^2$ evaluated with the selections $0.5 \le E_\nu < 6.0$ GeV and $M(p\pi^+) < 1.4$ GeV. The curve is the flux-averaged prediction of the Adler model with the dipole form factor and $M_A = 0.98$ GeV.

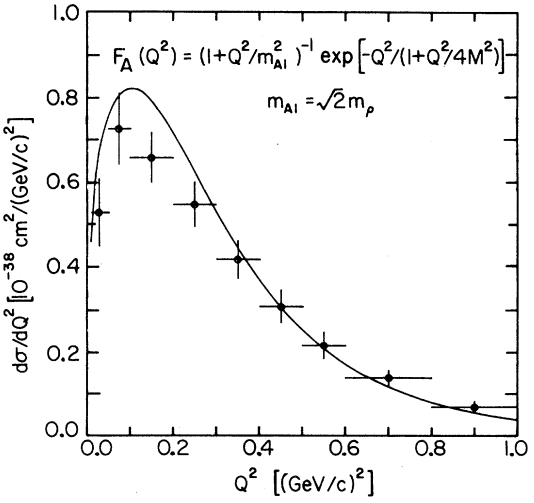

FIG. 13. Differential cross section $d\sigma/dQ^2$ evaluated with the selections $0.5 \le E_\nu < 6.0$ GeV and $M(p\pi^+) < 1.4$ GeV. The curve is the flux-averaged prediction of the Adler model with the Sehgal form factor as given in the figure legend.

TABLE IV. Form-factor fits. The model used is the extended Adler model. The events have the selection $0.5 \leq E_\nu < 6.0$ GeV and $M(p\pi^+) < 1.4$ GeV.

Q^2 Bin center [(GeV/c)^2]	$d\sigma/dQ^2$ Measured [10^{-38} cm^2/(GeV/c)^2]	$(d\sigma/dQ^2)^a$ $M_A=0.98$ GeV [10^{-38} cm^2/(GeV/c)^2]	χ^2	$(d\sigma/dQ^2)^b$ $M_A=0.95$ GeV [10^{-38} cm^2/(GeV/c)^2]	χ^2	$(d\sigma/dQ^2)^c$ [10^{-38} cm^2(GeV/c)^2]	χ^2
0.03	0.527±0.079	0.675	3.51	0.671	3.32	0.680	3.75
0.075	0.724±0.084	0.793	0.67	0.784	0.51	0.804	0.91
0.15	0.656±0.058	0.778	4.42	0.763	3.40	0.792	5.50
0.25	0.546±0.052	0.609	1.47	0.593	0.82	0.623	2.19
0.35	0.417±0.045	0.433	0.13	0.419	0.00	0.443	0.33
0.45	0.307±0.038	0.299	0.04	0.288	0.25	0.305	0.00
0.55	0.215±0.032	0.204	0.12	0.196	0.35	0.208	0.05
0.70	0.138±0.018	0.115	1.63	0.110	2.42	0.117	1.36
0.90	0.069±0.013	0.079	0.59	0.053	1.51	0.055	1.16
$\sum\chi^2$/DF			12.58/8		12.58/9		15.25/9
All Q^2	$\langle\sigma\rangle$ Measured	$(\langle\sigma\rangle)^a$ (10^{-38} cm^2) $M_A=0.98$ GeV		$(\langle\sigma\rangle)^b$ (10^{-38} cm^2) $M_A=0.95$ GeV		$(\langle\sigma\rangle)^c$(10^{-38} cm^2)	
	0.328±0.015	0.350	2.15	0.339	0.54	0.363	5.45

[a] $F_A(Q^2)=(1+Q^2/M_A{}^2)^{-2}$, M_A is a free parameter.
[b] $F_A(Q^2)=(1+Q^2/M_A{}^2)^{-2}$, M_A is fixed at 0.95 GeV.
[c] $F_A(Q^2)=(1+Q^2/m_{A_1}{}^2)^{-1}\exp[-Q^2/(1+Q^2/4M^2)]$, $m_{A_1}=\sqrt{2}m_\rho$.

The extended Adler model with $M_A = 0.95$ GeV has been used to generate the curves which are compared with our data in Figs. 1, 5, 9, and 12. Reasonable agreement with the data is found in all cases.

C. π^+ angular distributions from the final state $\mu^- p\pi^+$

The π^+ angular distributions in the $p\pi^+$ rest frame is usually displayed in the coordinate system defined in Fig. 14. The θ and ϕ distributions for $M(p\pi^+) < 1.4$ GeV are displayed in Figs. 15 and 16, respectively. Once again the curves are the area-normalized predictions of the extended Adler model with $M_A = 0.95$ GeV. The forward-backward and left-right asymmetries, where forward is $0 < \cos\theta < 1.0$, and right is $0 < \phi < 180°$ are measured. The forward-backward asymmetry is

$$\alpha_{\text{exp}} = \frac{N_F - N_B}{N_F + N_B} = -0.051 \pm 0.035 ,$$

and the left-right asymmetry is

$$\beta_{\text{exp}} = \frac{N_L - N_R}{N_L + N_R} = 0.053 \pm 0.035 .$$

The extended Adler model predicts these asym-

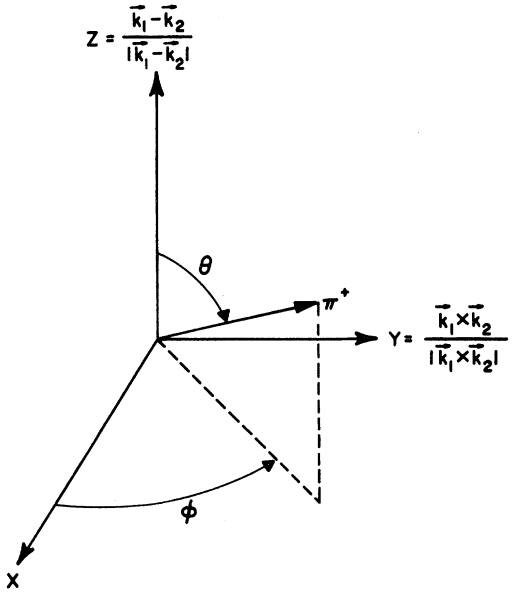

FIG. 14. Definition of the azimuthal ϕ and polar θ angles in the Adler system. $\vec{k}_1$ and $\vec{k}_2$ are vectors along the ν and μ^- directions, respectively, in the $N\pi$ rest system.

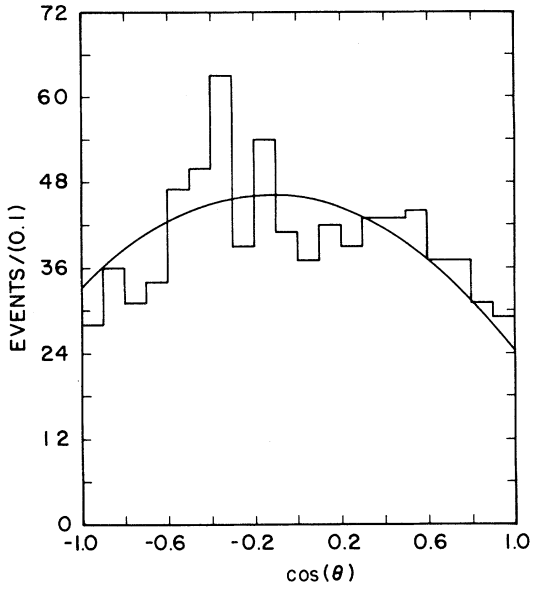

FIG. 15. Distribution of events in the pion polar angle $\cos\theta$ for the final state $\mu^- p\pi^+$, with $M(p\pi^+) < 1.4$ GeV. The curve is the area-normalized prediction of the Adler model.

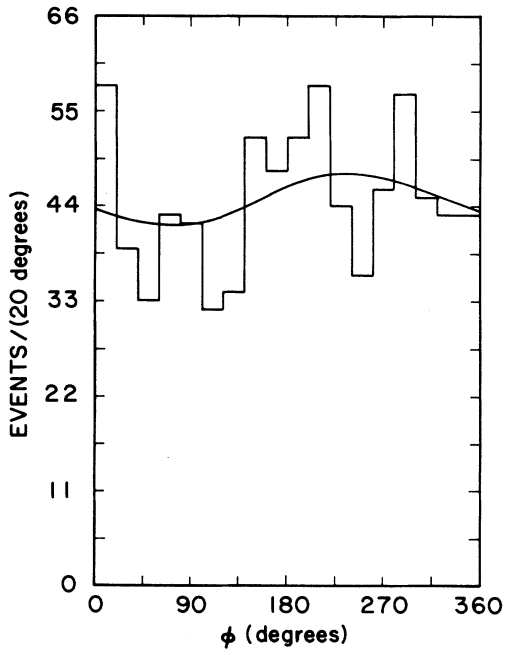

FIG. 16. Distribution of events in the pion azimuthal angle ϕ for the final state $\mu^- p\pi^+$, with $M(p\pi^+) < 1.4$ GeV. The curve is the area-normalized prediction of the Adler model.

TABLE V. $\Delta^{++}(1232)$ density matrix elements.

Angular or Q^2 range	$\tilde{\rho}_{33}$	$\tilde{\rho}_{31}$	$\tilde{\rho}_{3-1}$	Events
$-1.0 \leq \cos\theta^* \leq 1.0$	0.661±0.036	−0.107±0.040	−0.088±0.042	805
$-1.0 \leq \cos\theta^* < -0.4$	0.582±0.095	0.003±0.101	−0.144±0.102	125
$-0.4 \leq \cos\theta^* < 0.0$	0.768±0.084	−0.049±0.095	−0.073±0.107	141
$0.0 \leq \cos\theta^* < 0.4$	0.722±0.073	−0.011±0.087	−0.160±0.097	159
$0.4 \leq \cos\theta^* < 0.8$	0.704±0.064	−0.169±0.074	0.035±0.081	235
$0.8 \leq \cos\theta^* \leq 1.0$	0.488±0.090	−0.266±0.095	−0.176±0.090	145
$0.0 \leq Q^2 < 0.10$ (GeV/c)^2	0.523±0.086	−0.322±0.096	−0.138±0.093	145
$0.10 \leq Q^2 < 0.30$ (GeV/c)^2	0.649±0.061	−0.128±0.064	0.034±0.071	292
$0.30 \leq Q^2 < 0.50$ (GeV/c)^2	0.674±0.079	−0.017±0.088	−0.203±0.090	172
$0.50 \leq Q^2 < 1.00$ (GeV/c)^2	0.748±0.079	0.041±0.090	−0.162±0.098	160

metries to be

$$\alpha = -0.055, \quad \beta = +0.039 ,$$

and so both the sign and magnitude of the predicted asymmetries are in agreement with our measurements. A nonzero value for these asymmetries would indicate a nonresonant $I=\frac{3}{2}$ background amplitude interfering with the Δ resonance. Our result may be contrasted with the high-energy data,[17] where the extended Adler model is in poor agreement with the π^+ angular distributions. The Fogli calculation, which incorporates a background amplitude, is more successful in describing the observed π^+ angular distributions at high energies, as well as preserving the agreement with our results.

If the interfering nonresonant $I=\frac{3}{2}$ background is neglected, and assuming time-reversal invariance holds in the Δ^{++} production, then the Δ^{++} decay distribution is given by

$$\frac{d\sigma}{d\Omega} = \frac{\sigma}{\sqrt{4\pi}} \left[Y_0^0 - \frac{2}{\sqrt{5}}(\tilde{\rho}_{33} - \tfrac{1}{2}) Y_2^0 + \frac{4}{\sqrt{10}} \tilde{\rho}_{31} \mathrm{Re} Y_2^1 - \frac{4}{\sqrt{10}} \tilde{\rho}_{3-1} \mathrm{Re} Y_2^2 \right] , \tag{9}$$

where Y_L^M are spherical harmonic functions and $\tilde{\rho}_{mn}$ are the density-matrix elements. Table V gives the experimental values for the three Δ^{++} density-matrix elements for different $\cos\theta^*$ and Q^2 intervals for the region $M(p\pi^+) < 1.4$ GeV. Table VI gives the experimental values of the "illegal" Y_L^M moments. All are consistent with zero.

D. Isospin analysis

Assuming the $\Delta S=0$ weak hadronic charged current transforms as an isovector, we can write the amplitudes for the final states $\mu^- p\pi^+$, $\mu^- p\pi^0$, and $\mu^- n\pi^+$ in terms of the two reduced amplitudes A_1 and A_3, which correspond to the $I=\frac{1}{2}$ $I=\frac{3}{2}$ states of the nucleon-pion system. The amplitudes are

$$A(\mu^- p\pi^+) = A_3 , \tag{10}$$

$$A(\mu^- p\pi^0) = \frac{\sqrt{2}}{3} A_3 - \frac{\sqrt{2}}{3} A_1 , \tag{11}$$

$$A(\mu^- n\pi^+) = \tfrac{1}{3} A_3 + \tfrac{2}{3} A_1 . \tag{12}$$

In our previous studies,[1] we considered the possibility of an isotensor exchange amplitude B_3 feeding the $I=\frac{3}{2}$ nucleon-pion resonant state.[19] Our data satisfy the triangular inequalities resulting

TABLE VI. "Illegal" Y_L^M moments for the $\Delta^{++}(1232)$ decay.

	$\langle Y_L^M \rangle$		$\langle Y_L^M \rangle$
Y_1^0	−0.006±0.009	$\mathrm{Re}Y_3^1$	−0.002±0.007
$\mathrm{Re}Y_1^1$	0.006±0.007	$\mathrm{Im}Y_3^1$	−0.003±0.007
$\mathrm{Im}Y_1^1$	0.014±0.007	$\mathrm{Re}Y_3^2$	−0.006±0.007
$\mathrm{Im}Y_2^1$	−0.008±0.007	$\mathrm{Im}Y_3^2$	−0.003±0.007
$\mathrm{Im}Y_2^2$	−0.000±0.007	$\mathrm{Re}Y_3^3$	0.010±0.007
Y_3^0	0.012±0.010	$\mathrm{Im}Y_3^3$	−0.004±0.007

TABLE VII. The observed number of events and the corrected number of events for the isospin analysis. The events have the selection $E_\nu < 1.5$ GeV.

Reaction	Observed fits	No mass cut	$M_{N\pi} < 1.4$ GeV	$M_{N\pi} < 1.6$ GeV
$\mu^- p\pi^+$	573	730.6±34.4	716.5±34.0	729.3±34.3
$\mu^- p\pi^0$	202.2[a]	272.8±25.8	236.2±23.0	261.8±24.9
$\mu^- n\pi^+$	206.2[a]	255.8±22.0	225.6±19.3	254.8±20.9

[a]Number of fits observed are noninteger due to resolution of ambiguities.

from Eqs. (10)—(12), hence the data do not require a B_3 term, and so we ignore this possibility.

We restrict the events of reaction (1) to the 730.6 corrected events which originate in the same film sample used for reactions (2) and (3) and which satisfy the energy cut $E_\nu < 1.5$ GeV.

If $A_3 >> A_1$, then the following relations would hold:

$$R^+ = \sigma(\mu^- n\pi^+)/\sigma(\mu^- p\pi^0) = \tfrac{1}{2} , \quad (13)$$

$$R^{++} = [\sigma(\mu^- p\pi^0) + \sigma(\mu^- n\pi^+)]/\sigma(\mu^- p\pi^+) = \tfrac{1}{3} , \quad (14)$$

$$R_1 = \sigma(\mu^- p\pi^0)/\sigma(\mu^- p\pi^+) = \tfrac{2}{9} , \quad (15)$$

$$R_2 = \sigma(\mu^- n\pi^+)/\sigma(\mu^- p\pi^+) = \tfrac{1}{9} . \quad (16)$$

For nucleon-pion masses less than 1.4 GeV (see Table VII), we measure $R^+ = 0.96 \pm 0.12$, $R^{++} = 0.64 \pm 0.05$, $R_1 = 0.33 \pm 0.04$, and $R_2 = 0.31 \pm 0.03$. Therefore, the A_1 amplitude is needed in addition to the A_3 amplitude.

Solving Eqs. (10)—(12) for the relative magnitude of the amplitudes, $R = |A_1|/|A_3|$, and their relative phase ϕ, we measure for nucleon-pion masses less than 1.4 GeV, $R = 0.68 \pm 0.04$ and $\phi = 90.7° \pm 4.6°$. These results are consistent with a resonant $I = \frac{3}{2}$ amplitude in the presence of a large nonresonant $I = \frac{1}{2}$ background.

We have repeated the calculation, both for nucleon-pion masses less than 1.6 GeV and for the total data sample. Table VII lists the corrected total of observed events after all experimental corrections have been made for the various mass cuts. Our results are displayed in Fig. 17 and are tabulated in Table VIII along with the predictions of the extended Adler,[11] Fogli,[12] and Rein[13] models for the 1.4 and 1.6 GeV mass cuts. The data agree reasonably well with the model calculations as well as with the recent experimental results from the BNL 7-ft bubble chamber.[20]

IV. SUMMARY

The extended Adler model agrees reasonably with all aspects of our data. We measured the mass (M_A) of the axial-vector elastic form factor using the extended Adler model. Our result of $M_A = 0.98^{+0.06}_{-0.03}$ GeV, based on a maximum-likelihood fit to the $\mu^- p\pi^+$ data, is in agreement with the direct measurement of $M_A = 0.95 \pm 0.09$ GeV obtained from the reaction $\nu d \to \mu^- pp_s$. Our data agree equally well with a dipole form factor and the alternate parametrization suggested by Sehgal.

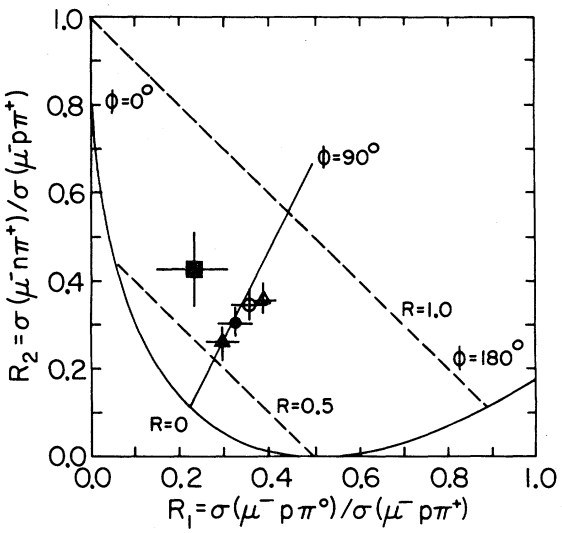

FIG. 17. Plot of the cross-section ratios $R_1 = \sigma(\mu^- p\pi^0)/\sigma(\mu^- p\pi^+)$ and $R_2 = \sigma(\mu^- n\pi^+)/\sigma(\mu^- p\pi^+)$. The dashed straight lines and the solid curves correspond to constant values of $R = |A_1|/|A_3|$ and the relative phase angle ϕ, respectively. This experiment is denoted by circular symbols. Also shown are the CERN PS Gargamelle (Ref. 15, square) and BNL 7-ft (Ref. 20, triangles) results. Solid symbols indicate that the ratios have been evaluated for $M(N\pi) < 1.4$ GeV and open symbols $M(N\pi) < 1.6$ GeV.

TABLE VIII. Results of the isospin analysis.

Quantity	$M(N\pi) < 1.4$ GeV Adler	Fogli and Nardulli	Rein and Sehgal	Experiment	$M(N\pi) < 1.6$ GeV Fogli and Nardulli	Experiment
R^+	0.78	0.66	0.94	0.96 ± 0.12	0.76	0.97 ± 0.12
R^{++}	0.59	0.57	0.61	0.64 ± 0.05	0.62	0.71 ± 0.06
R_1	0.33	0.34	0.31	0.33 ± 0.04	0.35	0.36 ± 0.04
R_2	0.26	0.23	0.29	0.31 ± 0.03	0.27	0.35 ± 0.03
R	0.61	0.59	0.64	0.68 ± 0.04	0.65	0.75 ± 0.04
ϕ	94.9°	99.2°	90.3°	$90.7°\pm4.6°$	96.6°	$92.0°\pm4.1°$

ACKNOWLEDGMENTS

We would like to thank the 12-ft bubble-chamber crew and the scanning and measuring staffs at the participating institutions for their help. This work was supported in part by the U. S. Department of Energy and the National Science Foundation.

*Present address: Center for Naval Analyses, Alexandria, VA 22311.
†Present address: Louisiana State University, Baton Rouge, LA 70803.
‡Permanent address: Valparaiso University, Valparaiso, IN 46383.
§Present address: Bell Telephone Laboratories, Naperville, IL 60540.
||Present address: Rutgers University, New Brunswick, NJ 08903.
¶Permanent address: Technion, Haifa, Israel.
**Present address: U. S. Department of Energy, Washington, D. C. 20545.
††Present address: Gulf Oil Corp, Harmerville, PA 15024.
‡‡Present address: University of Toronto, Toronto, Ontario, Canada.

[1]S. J. Barish *et al.*, Phys. Rev. D 19, 2521 (1979).
[2]S. J. Barish *et al.*, Phys. Rev. D 16, 3103 (1977).
[3]For additional details, see G. M. Radecky, Ph.D. thesis, Purdue University, 1980 (unpublished).
[4]M. Derrick *et al.*, Phys. Rev. D 23, 569 (1981).
[5]M. Derrick *et al.*, Phys. Lett. 92B, 363 (1980).
[6]S. J. Barish *et al.*, Report No. ANL-HEP-CP-81-26 (unpublished).
[7]S. E. Derenzo and R. H. Hildebrand, Nucl. Instrum. Methods 69, 287 (1969); J. Cochrane *et al.*, *ibid.* 160, 503 (1979).
[8]S. J. Barish *et al.*, Phys. Lett. 91B, 161 (1980).
[9]Y. Cho *et al.*, Phys. Rev. D 4, 1967 (1971).
[10]S. M. Berman and M. Veltman, Nuovo Cimento 38, 993 (1965); C. H. Albright and L. S. Liu, Phys. Rev. Lett. 13, 673, (1964); 14, 324 (1964); Phys. Rev. B104, 748 (1965); C. W. Kim, Nuovo Cimento 37, 142 (1965); Ph. Salin, *ibid.* 48A, 506 (1967); J. Bijtebier, Nucl. Phys. B21, 158 (1970); P. A. Zucker, Phys. Rev. D 4, 3350 (1971); P. Andreadis *et al.*, Ann. Phys. (N.Y.) 88, 242 (1974); 97, 576(E) (1976); F. Ravndal, Lett. Nuovo Cimento 3, 631 (1972); Nuovo Cimento 18A, 385 (1973); T. Alevizos *et al.*, J. Phys. G 3, 1179 (1979); P. A. Schreiner and F. von Hippel, Nucl. Phys. B58, 333 (1973).
[11]S. L. Adler, Ann. Phys. (N.Y.) 50, 189 (1968); Phys. Rev. D 12, 2644 (1975).
[12]G. L. Fogli and G. Nardulli, Nucl. Phys. B160, 116 (1979).
[13]D. Rein and L. M. Sehgal, Physikalisches Institut Techniche Hochschule Aachen report (unpublished).
[14]M. Block *et al.*, Phys. Lett. 12, 281 (1964); I. Budagov *et al.*, Phys. Lett. 29B, 524 (1969); W. Lerche *et al.*, *ibid.* 78B, 510 (1978).
[15]M. Pohl *et al.*, Lett. Nuovo Cimento 24, 540 (1979).
[16]N. J. Baker *et al.*, Phys. Rev. D 23, 2499 (1981) and reference cited therein.
[17]J. Bell *et al.*, Phys. Rev. Lett. 41, 1012 (1978); P. Allen *et al.*, Nucl. Phys. B176, 269 (1980).
[18]L. M. Sehgal, in *Proceedings of the European Physical Society International Conference on High Energy Physics, Geneva, 1979,* edited by A. Zichichi (CERN, Geneva, 1980), p. 98.
[19]R. J. Oakes and H. Primakoff, Phys. Rev. D 7, 275 (1973).
[20]N. J. Baker *et al.*, Phys. Rev. D 23, 2495 (1981).